JVST B
Journal of Vacuum Science & Technology B

ARTICLE

pubs.aip.org/avs/jvb

Remote plasma-enhanced chemical vapor deposition of GeSn on Si (100), Si (111), sapphire, and fused silica substrates

Cite as: J. Vac. Sci. Technol. B 42, 052204 (2024); doi: 10.1116/6.0003689
Submitted: 15 April 2024 · Accepted: 24 July 2024 ·
Published Online: 20 August 2024

View Online Export Citation CrossMark

B. Claflin,[1] G. J. Grzybowski,[2,a)] S. Zollner,[3] B. R. Rogers,[4] T. A. Cooper,[2] and D. C. Look[5]

AFFILIATIONS

[1]Air Force Research Laboratory, Sensors Directorate, Wright-Patterson Air Force Base, Ohio 45433
[2]KBR, 3725 Pentagon Blvd., Suite 100, Beavercreek, Ohio 45431
[3]Department of Physics, New Mexico State University, Las Cruces, New Mexico 88003
[4]Department of Chemical and Biomolecular Engineering, Vanderbilt University, Nashville, Tennessee 37235
[5]Semiconductor Research Center, Wright State University, Dayton, Ohio 45435

Note: This paper is part of the 2024 Special Topic Collection on Developing SiGeSn Technology: Materials and Devices.

[a)]Electronic mail: gordon.grzybowski@us.kbr.com

ABSTRACT

GeSn films were simultaneously deposited on Si (100), Si (111), c-plane sapphire (Al_2O_3), and fused silica substrates to investigate the impact of the substrate on the resulting GeSn film. The electronic, structural, and optical properties of these films were characterized by temperature-dependent Hall-effect measurements, x-ray diffractometry, secondary ion mass spectrometry, and variable angle spectroscopic ellipsometry. All films were polycrystalline with varying degrees of texturing. The film on Si (100) contained only GeSn (100) grains, 40.4 nm in diameter. The film deposited on Si (111) contained primarily GeSn (111) grains, 36.4 nm in diameter. Both films deposited on silicon substrates were fully relaxed. The layer deposited on Al_2O_3 contained primarily GeSn (111) grains, 41.3 nm in diameter. The film deposited on fused silica was not textured, and the average grain size was 35.0 nm. All films contained ~5.6 at. % Sn throughout the layer, except for the film deposited on Al_2O_3, which contained 7.5% Sn. The films deposited on Si (111), Al_2O_3, and fused silica exhibit p-type conduction over the entire temperature range, 10–325 K, while the layer deposited on the Si (100) substrate shows a mixed conduction transition from p-type at low temperature to n-type above 220 K. From ~175 to 260 K, both holes and electrons contribute to conduction. Texturing of the GeSn film on Si (100) was the only characteristic that set this film apart from the other three films, suggesting that something related to GeSn (100) crystal orientation causes this transition from p- to n-type conduction.

I. INTRODUCTION

Development of GeSn alloys for optoelectronic applications in the midwave infrared (MWIR) spectral range has progressed substantially over the last decade. Emitters and detectors based on GeSn have been demonstrated, including light emitting diodes[1–4] (LEDs), optically[5–8] and electrically[9–11] pumped lasers, as well as p–i–n photodiodes[12–16] and prototype arrays,[17,18] respectively. These efforts are motivated by the fact that for Sn concentrations exceeding 6%–7% (depending on strain in the material), GeSn has a direct bandgap,[19–23] making both emission and detection processes more efficient. Transistors have also been fabricated[24–27] to take advantage of the higher carrier mobilities seen in GeSn[28,29] compared to Si-based devices.

Continued development of this technology faces two significant challenges: (i) the limited thermodynamic solubility[30] of Sn in Ge, which is less than 1 at. % at room temperature and (ii) the large lattice mismatch between GeSn films and Si or Ge substrates, which induces misfit and other dislocations to relieve the generated strain. To address the first of these challenges, low-temperature, nonequilibrium growth techniques such as molecular beam epitaxy[31–34] (MBE), chemical vapor deposition[35–38] (CVD), remote plasma-enhanced CVD[39,40] (RPECVD), and other more unconventional approaches[41–43] have been successfully implemented. To overcome the second challenge, thick Ge buffer layers[44,45] (also referred to as Ge "virtual substrates") or graded buffers[46] are frequently introduced between the GeSn layer and the Si substrate to reduce the lattice mismatch.

The most common substrate used for deposition of GeSn films is Si (100) because of the availability of cheap, large format substrates and a mature commercial-support infrastructure. It also offers the potential for monolithic integration with readout and control circuitry. Other common, low-cost substrates, such as Al_2O_3 and fused silica, are also useful for process development experiments or for applications that require electrical isolation, but they have been studied far less. There have been limited reports of GeSn growth on Si (111) substrates,[27,38,47–49] as well as on Al_2O_3.[50]

Most of our work developing RPECVD GeSn deposition processes[39,40] have been performed using Si (100) substrates. We have used temperature-dependent Hall-effect (TDH) measurements to investigate carrier concentrations and mobilities in some of the resulting GeSn films. The TDH analyses of these films show that holes dominate conduction at low temperatures while electrons dominate conduction at higher temperatures. These TDH observations have been consistent, independent of processing conditions, for GeSn films deposited on Si (100) substrates.

In this work, we use GeSn films simultaneously deposited via RPECVD on four different substrates, Si (100), Si (111), fused silicon, and sapphire, to investigate the observed p- to n-type conduction transition. Carrier concentrations and mobilities were determined using TDH while the structural and optical properties of these films were characterized using secondary ion mass spectroscopy (SIMS), variable angle spectroscopic ellipsometry (VASE), atomic force microscopy (AFM), and x-ray diffractometry (XRD).

II. EXPERIMENTAL DETAILS

Two-inch diameter wafers of Si (100), Si (111), c-plane Al_2O_3, and fused silica were cleaved into quarters. One quarter of each substrate was cleaned, placed on a single 2-in. diameter stainless steel sample holder, and immediately loaded into a custom-designed RPECVD reactor.[40] The silicon substrates were cleaned with a 1-min dilute HF etch, while a 10-min ozone treatment was used to clean the Al_2O_3 and fused silica substrates. The RPECVD process used 6% GeH_4 in He as the Ge source while Sn was supplied from liquid $SnCl_4$ in a bubbler using He as the carrier gas. A remote He plasma was excited via an inductively coupled quartz plasma tube mounted on top of the reactor chamber. A chamber pressure of 550 mTorr and a constant substrate temperature of 360 °C were maintained throughout the deposition. Additional details about the deposition process and equipment have been previously reported.[39,40]

TDH was measured using a LakeShore 7505 system on approximately 1 × 1 cm^2 van der Pauw structures with soldered indium contacts on the corners. Data were collected from 10 to 325 K using a 10 kG magnetic field.

X-ray diffractometry was performed using a PANalytical Empyrean x-ray diffractometer equipped with a copper source with 0.5° exit slit and a hybrid monochromator. Diffracted Cu $K\alpha_1$ x rays were collected with a PIXcel3D hybrid array detector with an automatic receiving slit and Soller slits. 2θ–ω line scans were acquired around the (004) reflection using the scanning line mode. Strain in films deposited on Si (100) and Si (111) were investigated using $(\bar{2}\bar{2}4)$ and (224) reciprocal space maps (RSM), respectively, collected in the static line mode.

Film composition was determined using SIMS performed by Evans Analytical Group. Film thickness and optical characteristics were determined via VASE analyses performed on a JA Woollam RC2 multichannel, dual rotating compensator ellipsometer. Data were collected from 210 to 2500 nm at angles of 55°, 60°, 65°, 70°, and 75°.

III. RESULTS AND DISCUSSION

Figure 1 presents results of the TDH measurements. Figure 1(a) shows resistivity versus temperature for the GeSn films deposited on each of the four substrates. Note that resistivities of the films deposited on Si (111), fused silica, and sapphire all decrease smoothly with increasing temperature. The resistivity of the GeSn film on fused silica decreased by 50% (from 0.1 to 0.05 Ω cm), while the resistivity curves of the films deposited on sapphire and Si (111) are very similar, each decreasing by 25% (from 0.06 to 0.045 Ω cm). A much larger, 95% (0.16 to 0.009 Ω cm) decrease in resistivity occurs for the GeSn film deposited on Si (100), with a sharp drop seen between 175 and 260 K.

Figure 1(b) plots the carrier concentrations and mobilities for GeSn films deposited on Si (111), fused silica, and sapphire substrates. These values were determined using a single-band analysis,[51] where conduction is dominated by either holes or electrons, as described by Eqs. (1)–(3),

$$R_H = -\frac{1}{qn}\,(\text{n-type}) \text{ or } R_H = \frac{1}{qp}\,(\text{p-type}), \tag{1}$$

$$\rho = \frac{1}{qn\mu_n}\,(\text{n-type}) \text{ or } \rho = \frac{1}{qp\mu_p}\,(\text{p-type}), \tag{2}$$

$$\mu = \frac{R_H}{\rho}, \tag{3}$$

where q is the magnitude of electric charge, n and p are carrier concentrations, and μ_n and μ_p are carrier mobilities. The sign of the Hall coefficient indicates the dominant carrier type, holes for $R_H > 0$ and electrons for $R_H < 0$. The Hall coefficients for the GeSn films deposited on Si (111), fused silica, and sapphire substrates films were all positive over the entire temperature range, indicating p-type conduction. The average hole concentrations were 5×10^{18}, 3.6×10^{18}, and $2.9 \times 10^{18}\ cm^{-3}$ for the films deposited on fused silica, sapphire, and Si (111), respectively. Carrier mobilities had the opposite trend, with the GeSn layer on Si (111) having the highest average value, 49.4 $cm^2\,V^{-1}\,s^{-1}$, followed by that on sapphire, 37.6 $cm^2\,V^{-1}\,s^{-1}$, and on fused silica, 17.8 $cm^2\,V^{-1}\,s^{-1}$.

The Hall carrier concentration and mobility curves, assuming single-band conduction, for GeSn on Si (100) are plotted in

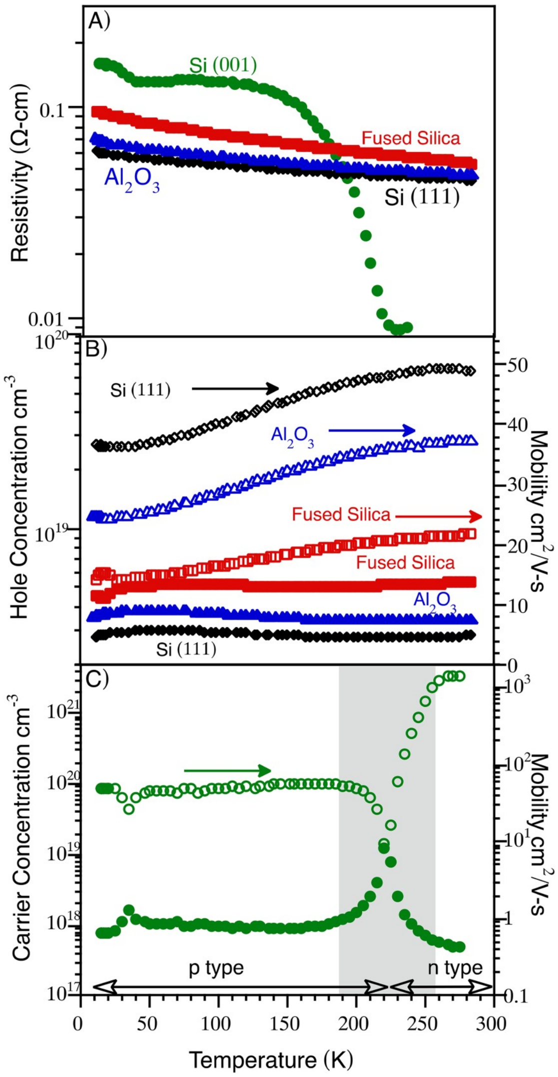

FIG. 1. Temperature-dependent resistivity, carrier concentration, and mobility curves determined assuming single-band conduction. (a) Resistivity vs sample temperature for GeSn films on Si(100), Si(111), fused silica, and sapphire substrates. (b) Hole concentration (filled symbols) and mobility (open symbols) for films on Si(111), fused silica, and sapphire substrates. (c) Carrier concentration (filled symbols) and mobilities (open symbols) in a film on a Si(100) substrate. Regions of p- and n-type conduction are determined by the sign of the Hall coefficient. The shaded area shows the approximate temperature range impacted by mixed band conduction.

Fig. 1(c). The sign of the Hall coefficient changes from positive to negative at a temperature between 220 and 225 K, indicating a mixed conduction transition. The impact of this multiband conduction is observed in a region on both sides of this p- to n-type transition, depicted by the gray box in Fig. 1(c). Note that the sharp decrease in resistivity of this film [Fig. 1(a)] also occurs in this temperature range. Neither holes nor electrons dominate the conduction in this region, and thus, the plotted concentration and mobility values determined using single-band analysis are not accurate. The apparent sharp rise in carrier concentration in this region is due to the use of a single-band conduction model [Eq. (1)] since R_H must pass through zero when going from positive to negative. Carrier concentration is inversely proportional to R_H and, thus, appears to rise sharply in the mixed conduction transition region. Likewise, the apparent rapid decrease in mobility seen between 175 and 260 K [Fig. 1(c)] is the result of the single-band analysis because mobility is proportional to R_H [Eq. (3)]. A two-band conduction model,[51] Eqs. (4) and (5), must be used to more accurately determine the carrier concentrations and mobilities in the mixed-conduction region

$$\rho = \frac{1}{q(n\mu_n + p\mu_p)}, \tag{4}$$

$$R_H = \frac{-n\mu_n^2 + p\mu_p^2}{q(n\mu_n + p\mu_p)^2}. \tag{5}$$

However, a basic TDH measurement does not provide enough data to determine the hole and electron concentrations and their mobilities from these equations. Carrier concentrations and mobilities for the GeSn sample deposited on the Si(100) substrate were relatively constant outside the transition region. Hole concentrations ranged from 7.8×10^{17} to 1.0×10^{18} cm^{-3} with an average mobility of 50.4 cm^{2}V^{-1} s^{-1} at temperatures far below the transition region, while electron concentrations ranged from 5.1×10^{17} to 7.0×10^{17} cm^{-3} with an average mobility of 1200 cm^{2}V^{-1} s^{-1} at higher temperatures. It is important to note that mobility plays a larger role than carrier concentration in determining the sign of R_H [Eq. (5)]. If the electron mobility is much larger than the hole mobility (as is the case here), the electron concentration can be orders of magnitude lower than the hole concentration and still dominate the conduction. There also appear to be indications of mixed conduction near 30 K; however, the contribution from electrons is not large enough to change the sign of R_H in this region.

Figure 2 presents SIMS depth profiles that were acquired to compare the compositions of the films deposited on the four substrates. To see the smaller Sn and O signals in each profile, the germanium signal has been divided by two. The Sn concentration in the bulk of each film is relatively constant. The GeSn films deposited on Si(100), Si (111), and fused silica all contain between 5.5 to 5.7 at. %, determined by averaging the Sn composition values measured at depths between 100 and 350 nm in the film. The film deposited on sapphire, however, had an average tin composition of 7.5 at. %. It is unclear what causes this increased level of Sn incorporation, especially considering all substrates were positioned on the same carrier and experienced the same deposition process. However, we have previously observed similar increased levels of Sn incorporation in films deposited on sapphire compared to films deposited on Si, in separate runs, using identical process conditions. It is possible that differences

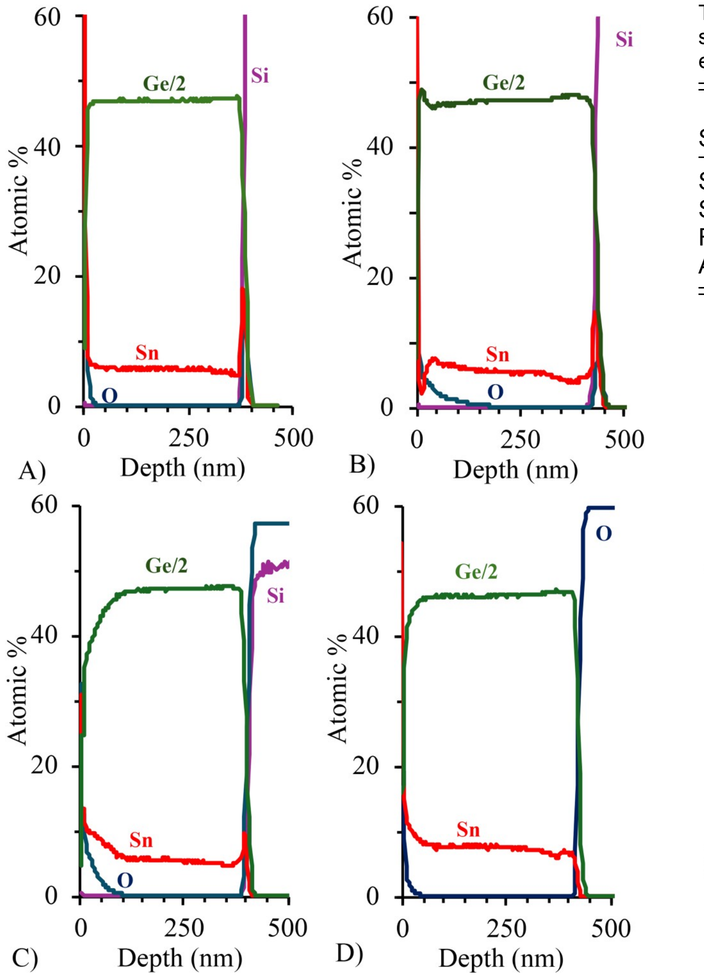

FIG. 2. SIMS depth profiles of GeSn films deposited simultaneously on different substrates. Note that the Ge signal has been divided by 2 to make the Sn and O signals more visible. (a) Si (100). Average Sn content ≈5.7 at. %, (b) Si (111). Average Sn content ≈5.5 at. %, (c) Fused silica. Average Sn content ≈5.5 at. %, and (d) sapphire. Average Sn content ≈7.5 at. %. Stated Sn content is the average content between depths of 100 and 350 nm in each film.

in thermal conductivity and radiative losses for the different substrates result in slightly different surface temperatures, which could affect the incorporation of Sn.

VASE was used to determine the thicknesses of the deposited films and to qualitatively compare their crystallinities. A two-step process was used to analyze the VASE data. First, film thickness and surface roughness were determined by fitting a model consisting of a substrate with a GeSn layer and a surface roughness layer to the ellipsometry data. The pseudodielectric function was then obtained by fixing the thickness and surface roughness values and fitting a B-spline function with nodes every 0.05 eV to the data. Results of these analyses are provided in Table I and Fig. 3. Table I contains film thickness and surface roughness determined from

TABLE I. GeSn film thickness and surface roughness determined from VASE analyses and AFM RMS roughness. Films were deposited simultaneously on four different substrates.

Substrate	Thickness (nm)	VASE surface roughness (nm)	AFM RMS roughness (nm)
Si (100)	398	13.8	12.6
Si (111)	425	14.7	10
Fused silica	467	19.5	9.2
Al_2O_3	466	9.4	9.3

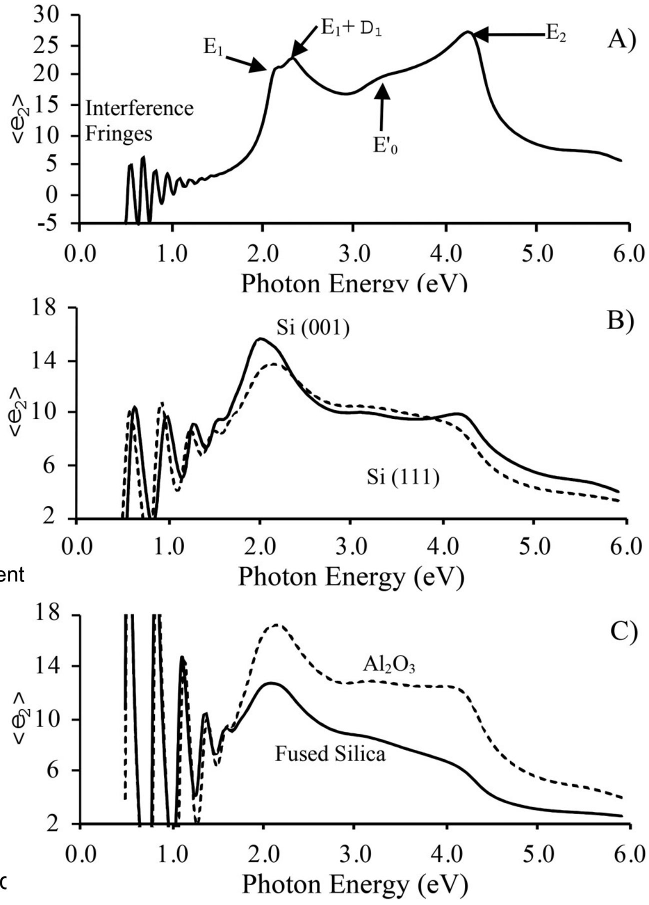

FIG. 3. Imaginary parts of pseudodielectric functions determined by VASE analyses of RPECVD films. (a) Results from an ≈1000 nm thick Ge film deposited on Si (100) for reference. Interference fringes are used to determine the film thickness. Critical points in the Ge band structure (E_1, $E_1 + \Delta_1$, $E_0^{\prime}$, and E_2) are shown. (b) Results from GeSn films deposited on Si (100) and Si (111). (c) Results from GeSn films deposited on fused silica and sapphire. Plots in (b) and (c) have been scaled to highlight the shape of the pseudodielectric functions above the interference fringes.

VASE analyses as well as root mean square (RMS) roughness determined from 10 × 10 μm^2 AFM images (Fig. S2 in the supplementary material).

Figure 3(a) plots the imaginary part of the pseudodielectric function for a pure germanium film deposited on a Si(100) substrate in our RPECVD system. Interference between photons reflecting off the Ge/Si interface and off the film's surface form the fringes observed below ~1.8 eV. These fringes are used to determine the film thickness. Photons with energies above ~2 eV do not penetrate through the entire film thickness due to the energy dependence of the absorption coefficient. Therefore, the spectrum at energies above ~2 eV provides information about the dielectric function of just the film, not the underlying substrate. The energies E_1, $E_1 + \Delta_1$, E_0^0, and E_2 are energy levels of critical transitions in the germanium band structure. The appearance of these peaks and shoulders in the dielectric function is an indication of good crystallinity. The shapes of the dielectric functions of Ge and GeSn are similar for the relatively low level of Sn incorporation in these samples. Figure 3(b) compares the imaginary part of pseudodielectric functions from GeSn films deposited on Si (100) and Si(111), while Fig. 3(c) compares the imaginary part of pseudodielectric functions for GeSn films deposited on fused silica and sapphire. The scales on these plots have been expanded to highlight the shape of the pseudodielectric function above the interference fringes. The shape of the pseudodielectric function of the film deposited on Si(100) is very similar to that of the germanium film presented in Fig. 3(a). The shapes of the pseudodielectric function of the films deposited on Si (111) and sapphire are similar, but their peaks are broader than those of the film on Si (100) and the Ge film. These observations suggest the film on Si (100) has better crystalline quality than that on Si(111) and sapphire. The shape of the pseudodielectric function for the film on fused silica is even broader and less defined, suggesting poorer crystalline quality.

Figure 4 presents XRD 2θ–ω scans to determine the crystal orientations present in the four GeSn films. Table II lists the position of the peaks, their corresponding d-spacings, and an estimate of their grain size determined by applying Scherrer's equation to the most intense peak present in each scan. The films deposited on Si (100) and sapphire had similar grain sizes, 40.4 and 41.3 nm, respectively. Films deposited on Si(111) and fused silica had smaller grains, 36.4 and 35.0 nm, respectively.

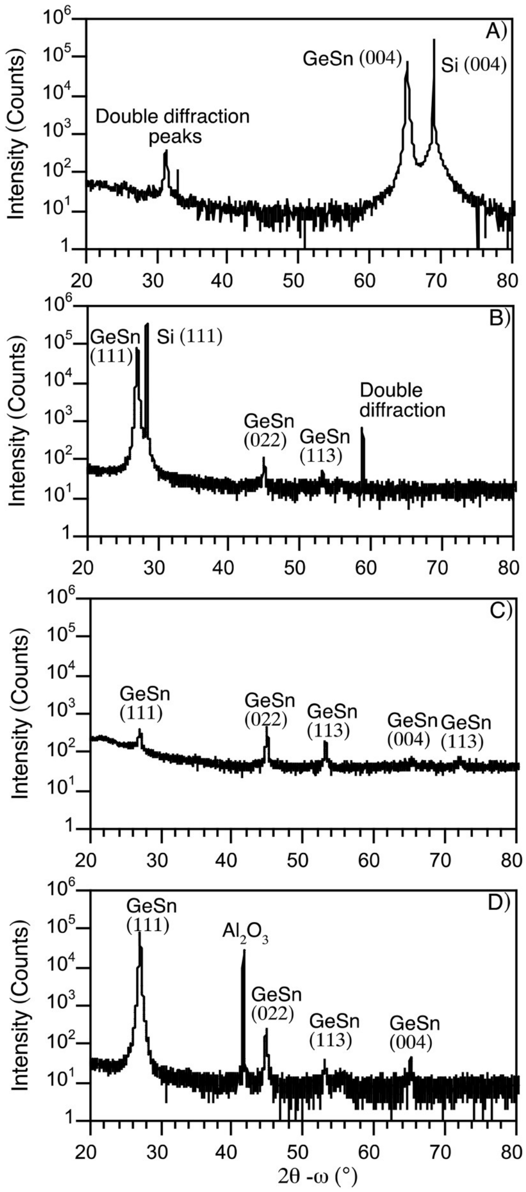

FIG. 4. X-ray diffraction 2θ–ω scans of GeSn layers deposited simultaneously on (a) Si(100), (b) Si(111), (c) fused silica, and (d) Al_2O_3 substrates.

TABLE II. Peak position, d-spacing, and film grain size determined from 2θ–ω scans of GeSn films on Si(100), Si (111), fused silica, and Al_2O_3 substrates. The grain size was estimated applying Scherrer's equation to the most intense GeSn peak present in each scan.

GeSn plane	Measurement	Substrate Si (100)	 Si (111)	 Fused Silica	 Sapphire
(111)	Position (deg)	—	27.09	27.02	27.02
	d-spacing (Å)	—	3.289	3.297	32.98
	Grain size (nm)	—	36.43	—	41.3
(022)	Position (deg)	—	44.97	44.95	44.84
	d-spacing (Å)	—	2.014	2.015	2.020
	Grain size (nm)	—	—	35.0	—
(113)	Position (deg)	—	53.24	53.21	53.17
	d-spacing (Å)	—	1.719	1.720	1.721
(004)	Position (deg)	65.33	—	65.43	65.23
	d-spacing (Å)	1.427	—	1.425	1.429
	Grain size (nm)	40.4	—	—	—
(133)	Position (deg)	—	—	72.21	—
	d-spacing (Å)	—	—	1.307	—

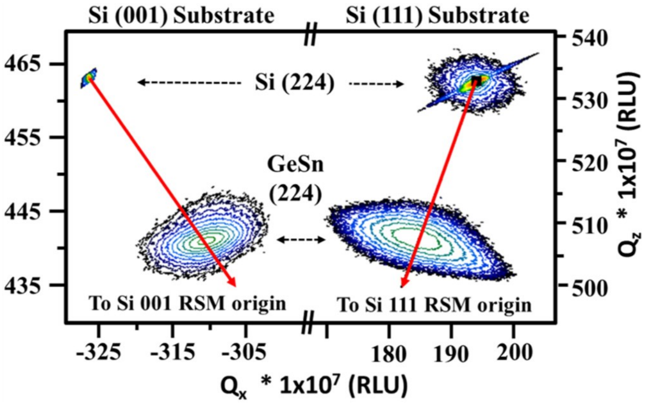

FIG.5. X-ray RSM analyses around $(\bar{2}\bar{2}4)$ and (224) reflections of GeSn films deposited on Si(100) and Si(111) show the films are fully relaxed.

While each of the GeSn films is polycrystalline, they have different degrees of texturing. As seen in Fig. 4(a), GeSn (004) is the only peak present in the 2θ–ω scan from the GeSn film on Si (100). The lack of other GeSn peaks suggests that this film is highly textured, with all grains oriented with GeSn (100) planes parallel to the surface. The 2θ–ω scans from the GeSn film on Si (111), shown in Fig. 4(b), and from the film on sapphire, shown in Fig. 4(d), contain an intense GeSn (111) peak with other, orders of magnitude smaller peaks, suggesting the grains in these films are primarily oriented with the (111) plane parallel to the surface. In contrast, the peaks in the 2θ–ω scan of the GeSn film deposited on fused silica, Fig. 4(c), all have very low intensity, suggesting almost random orientation of the grains in this film. Note that peaks due to double diffraction from silicon are present in the 2θ–ω scan of films deposited on both silicon substrates. Pole figures were used (Fig. S1 in the supplementary material) to confirm that these are double diffraction peaks and not Sn peaks with different orientation.

Figure 5 shows RSMs around the $(\bar{2}\bar{2}4)$ and (224) reflections acquired from films deposited on Si(100) and Si(111) substrates, respectively, to determine the extent of film relaxation. The GeSn peak for each film is centered on its respective silicon relaxation line, shown in red, indicating both films are fully relaxed.

IV. SUMMARY AND CONCLUSIONS

Characteristics of GeSn films simultaneously deposited via RPECVD on Si (100), Si (111), fused silica, and sapphire were compared to evaluate the impact of the substrate on the deposited film. The GeSn film deposited on Si(100) exhibited a p- to n-type mixed conduction transition around 220 K, but the films deposited on all the other substrates exhibited p-type conduction for all temperatures. Interactions between the GeSn film and substrate are unlikely to cause the conduction type transition since only the film on Si (100) exhibited this behavior, not the film on Si (111). The Sn incorporation in the films can also be ruled out since the films on Si (111) and fused silica had similar Sn content to the film deposited on Si (100). The crystallinity of films on Si (100), Si (111), and sapphire were similar, and, therefore, crystallinity is also not the cause of the observed type conversion. Texturing of the GeSn film on Si(100) is different than that of the other films. The film on Si (100) has perfect (100) texturing, while films on Si (111) and sapphire have primarily (111) texturing, and the film on fused silica is randomly oriented. Since film texture is the only characteristic of these films that differentiates the GeSn film on Si (100) from the films on other substrates, and the film on Si (100) is the only one that exhibits mixed conduction transition, the (100) orientation of the GeSn film is likely to be responsible for the multiband conduction observed in TDH analysis. More work is needed to understand how GeSn crystal orientation can lead to mixed-band conduction in these films.

SUPPLEMENTARY MATERIAL

Figure S-1 contains an XRD pole figure of 2θ–ω versus w near the Si (100) double diffraction peaks collected from a RPECVD GeSn film on an Si (100) substrate. The figure shows that the intensity changes with sample rotation (w), indicating a case of multiple diffraction. Figure S-1 contains AFM images, 10 × 10 μm^2 surfaces of RPECVD GeSn films deposited on four different substrates.

ACKNOWLEDGMENTS

This work was supported by AFOSR LRIR Nos. 19RYCOR032 and 24RYCOR012 (G. Pomrenke and W. Miller, respectively) as well as AFOSR Summer Faculty Fellowship Program (Contract Nos. FA8750-15-3-6003, FA9550-15-0001, and FA9550-20-F-0005). The research performed by G.J.G. at the Air Force Research Laboratory was supported by Contract Award No. FA807518D1005. This material is also based upon work supported by the National Science Foundation (NSF) under Award No. DMR-2235447.

AUTHOR DECLARATIONS

Conflict of Interest

The Authors declare that there are no conflicts of interest.

Author Contributions

All authors contributed equally to this work.

B. Claflin: Conceptualization (equal); Formal analysis (equal); Funding acquisition (equal); Investigation (equal); Methodology (equal); Project administration (equal); Resources (equal); Supervision (equal); Visualization (equal); Writing – original draft (equal); Writing – review & editing (equal). G. J. Grzybowski: Conceptualization (equal); Formal analysis (equal); Funding acquisition (equal); Investigation (equal); Methodology (equal); Project administration (equal); Resources (equal); Supervision (equal); Visualization (equal); Writing – original draft (equal); Writing – review & editing (equal). S. Zollner: Conceptualization (equal); Formal analysis (equal); Funding acquisition (equal); Investigation (equal); Methodology (equal); Project administration (equal); Resources (equal); Supervision (equal); Visualization (equal);

Writing – original draft (equal); Writing – review & editing (equal). B. R. Rogers: Formal analysis (equal); Visualization (equal); Writing – review & editing (equal). T. A. Cooper: Conceptualization (equal); Formal analysis (equal); Funding acquisition (equal); Investigation (equal); Methodology (equal); Project administration (equal); Resources (equal); Supervision (equal); Visualization (equal); Writing – original draft (equal); Writing – review & editing (equal). D. C. Look: Conceptualization (equal); Formal analysis (equal); Funding acquisition (equal); Investigation (equal); Methodology (equal); Project administration (equal); Resources (equal); Supervision (equal); Visualization (equal); Writing – original draft (equal); Writing – review & editing (equal).

DATA AVAILABILITY

The data that support the findings of this study are available within the article.

REFERENCES

[1] R. Roucka, J. Mathews, R. T. Beeler, J. Tolle, J. Kouvetakis, and J. Menéndez, Appl. Phys. Lett. 98, 061109 (2011).

[2] Y. Y. Zhou et al., J. Appl. Phys. 120, 023102 (2016).

[3] J. D. Gallagher, C. L. Senaratne, P. Sims, T. Aoki, J. Menéndez, and J. Kouvetakis, Appl. Phys. Lett. 106, 091103 (2015).

[4] J. P. Gupta, N. Bhargava, S. Kim, T. Adam, and J. Kolodzey, Appl. Phys. Lett. 102, 251117 (2013).

[5] S. Wirths et al., Nat. Photonics 9, 88 (2015).

[6] S. Al-Kabi et al., Appl. Phys. Lett. 109, 171105 (2016).

[7] V. Reboud et al., Appl. Phys. Lett. 111, 092101 (2017).

[8] J. Margetis et al., ACS Photonics 5, 827 (2018).

[9] Y. Y. Zhou et al., Optica 7, 924 (2020).

[10] B. Marzban et al., Acs Photonics 10, 217 (2023).

[11] Y. Y. Zhou et al., Photonics Res. 10, 222 (2022).

[12] S. Q. Xu, W. Wang, Y. C. Huang, Y. Dong, S. Masudy-Panah, H. Wang, X. Gong, and Y. C. Yeo, Opt. Express 27, 5798 (2019).

[13] Y. H. Huang, G. E. Chang, H. Li, and H. H. Cheng, Opt. Lett. 42, 1652 (2017).

[14] H. S. Mączko, R. Kudrawiec, and M. Gladysiewicz, Sci. Rep. 6, 34082 (2016).

[15] S. Su et al., Opt. Express 19, 6400 (2011).

[16] J. Mathews, R. Roucka, J. Xie, S.-Q. Yu, J. Menéndez, and J. Kouvetakis, Appl. Phys. Lett. 95, 133506 (2009).

[17] H. Tran et al., Acs Photonics 6, 2807 (2019).

[18] C. Chang, H. Li, C. T. Ku, S. G. Yang, H. H. Cheng, J. Hendrickson, R. A. Soref, and G. Sun, Appl. Opt. 55, 10170 (2016).

[19] S. Zaima, O. Nakatsuka, N. Taoka, M. Kurosawa, W. Takeuchi, and M. Sakashita, Sci. Technol. Adv. Mater. 16, 043502 (2015).

[20] H. Lin, R. Chen, W. S. Lu, Y. J. Huo, T. I. Kamins, and J. S. Harris, Appl. Phys. Lett. 100, 102109 (2012).

[21] P. Moontragoon, R. A. Soref, and Z. Ikonic, J. Appl. Phys. 112, 073106 (2012).

[22] J. Mathews, R. T. Beeler, J. Tolle, C. Xu, R. Roucka, J. Kouvetakis, and J. Menéndez, Appl. Phys. Lett. 97, 2211912 (2010).

[23] S. Gupta, B. Magyari-Köpe, Y. Nishi, and K. C. Saraswat, J. Appl. Phys. 113, 073707 (2013).

[24] W. Wang et al., Opt. Express 26, 10305 (2018).

[25] Y. Liu, J. Yan, H. J. Wang, B. W. Cheng, and G. Q. Han, Int. J. Thermophys. 36, 980 (2015).

[26] P. F. Guo, R. Cheng, W. Wang, Z. Zhang, J. S. Pan, E. S. Tok, and Y. C. Yeo, ECS J. Solid State Sci. Technol. 3, Q162 (2014).

[27] G. Han et al., ECS Trans. 50, 943 (2013).

[28] J. D. Sau and M. L. Cohen, Phys. Rev. B 75, 045208 (2007).

[29] R. Cheng, Z. Chen, S. Yuan, M. Takenaka, S. Takagi, G. Han, and R. Zhang, J. Semicond. 42, 023101 (2021).

[30] R. W. Olesinski and G. J. Abbaschian, Bull. Alloy Phase Diagr. 5, 265 (1984).

[31] N. Bhargava, J. P. Gupta, N. Faleev, L. Wielunski, and J. Kolodzey, J. Electron. Mater. 46, 1620 (2017).

[32] M. Oehme, D. Buca, K. Kostecki, S. Wirths, B. Holländer, E. Kasper, and J. Schulze, J. Cryst. Growth 384, 71 (2013).

[33] E. Kasper, J. Werner, M. Oehme, S. Escoubas, N. Burle, and J. Schulze, Thin Solid Films 520, 3195 (2012).

[34] K. A. Bratland, Y. L. Foo, T. Spila, H. S. Seo, R. T. Haasch, P. Desjardins, and J. E. Greene, J. Appl. Phys. 97, 044904 (2005).

[35] J. Taraci et al., J. Am. Chem. Soc. 123, 10980 (2001).

[36] S. Wirths et al., Thin Solid Films 557, 183 (2014).

[37] J. Aubin and J. M. Hartmann, J. Cryst. Growth 482, 30 (2018).

[38] Y. H. Miao et al., Nanomaterials 11, 2556 (2021).

[39] B. Claflin, G. J. Grzybowski, M. E. Ware, S. Zollner, and A. M. Kiefer, Front. Mater. 7, 44 (2020).

[40] G. Grzybowski, M. E. Ware, A. Kiefer, and B. Claflin, J. Vac. Sci. Technol. B 38, 062209 (2020).

[41] H. F. Li, J. Brouillet, X. X. Wang, and J. F. Liu, Appl. Phys. Lett. 105, 201107 (2014).

[42] H. F. Li, J. Brouillet, A. Salas, X. X. Wang, and J. F. Liu, Opt. Mater. Express 3, 1385 (2013).

[43] H. Oka, T. Tomita, T. Hosoi, T. Shimura, and H. Watanabe, Appl. Phys. Express 11, 011304 (2018).

[44] M. Oehme, K. Kostecki, M. Schmid, F. Oliveira, E. Kasper, and J. Schulze, Thin Solid Films 557, 169 (2014).

[45] J. Werner, M. Oehme, M. Schmid, M. Kaschel, A. Schirmer, E. Kasper, and J. Schulze, Appl. Phys. Lett. 98, 061108 (2011).

[46] S. Abdi, S. Assali, M. R. M. Atalla, S. Koelling, J. M. Warrender, and O. Moutanabbir, J. Appl. Phys. 131, 105304 (2022).

[47] L. M. Wang, Y. C. Zhang, H. Sun, J. You, Y. H. Miao, Z. R. Dong, T. Liu, Z. M. Jiang, and H. Y. Hu, Nanoscale Adv. 3, 997 (2021).

[48] A. Nakatsuka, A. Yoshiasa, and T. Yamanaka, Acta Crystallogr., Sect. B 55, 266 (1999).

[49] K. Yu, D. L. Zhang, H. Cong, X. Zhang, Y. Zhao, B. W. Cheng, and C. B. Li, Presented at the 2016 IEEE 13th International Conference on Group IV Photonics (GFP) Shanghai, China, 2016.

[50] D. Gayakwad, D. Singh, R. Kumar, Y. I. Mazur, S. Q. Yu, G. J. Salamo, S. Mahapatra, and K. Khiangte, J. Cryst. Growth, 618, 127306 (2023).

[51] D. C. Look, Electrical Characterization of GaAs Materials and Devices (Wiley, Chichester, 1989).